ARTICLE

IRSp53 senses negative membrane curvature and phase separates along membrane tubules

Coline Prévost[1,2,3,4], Hongxia Zhao[5], John Manzi[1,2,3], Emmanuel Lemichez[6], Pekka Lappalainen[5], Andrew Callan-Jones[7,4,*] & Patricia Bassereau[1,2,3,*]

BAR domain proteins contribute to membrane deformation in diverse cellular processes. The inverted-BAR (I-BAR) protein IRSp53, for instance, is found on the inner leaflet of the tubular membrane of filopodia; however its role in the formation of these structures is incompletely understood. Here we develop an original assay in which proteins are encapsulated in giant unilamellar vesicles connected to membrane nanotubes. Our results demonstrate that I-BAR dimers sense negative membrane curvature. Experiment and theory reveal that the I-BAR displays a non-monotonic sorting with curvature, and expands the tube at high imposed tension while constricting it at low tension. Strikingly, at low protein density and tension, protein-rich domains appear along the tube. This peculiar behaviour is due to the shallow intrinsic curvature of I-BAR dimers. It allows constriction of weakly curved membranes coupled to local protein enrichment at biologically relevant conditions. This might explain how IRSp53 contributes *in vivo* to the initiation of filopodia.

[1] Institut Curie, Centre de Recherche, 75248 Paris Cedex 05, France. [2] CNRS, Physico-Chimie Curie, UMR 168, 75248 Paris Cedex 05, France. [3] Université Pierre et Marie Curie, 75252 Paris Cedex 05, France. [4] Université Paris-Diderot, 75205 Paris Cedex 05, France. [5] Institute of Biotechnology, University of Helsinki, 00014 Helsinki, Finland. [6] INSERM, U1065, UNSA, Centre Méditerranéen de Médecine Moléculaire, C3M, 06204 Nice Cedex 3, France. [7] CNRS, Laboratoire Matière et Systèmes Complexes, UMR 7057, 75205 Paris Cedex 13, France. * These authors contributed equally to this work. Correspondence and requests for materials should be addressed to P.B. (email: patricia.bassereau@curie.fr) or to A.C.-J. (email: andrew.callan-jones@univ-paris-diderot.fr).

BAR (Bin/amphiphysin/Rvs) domain proteins are linked to essential cellular processes involving membrane remodelling, such as cell migration and membrane trafficking[1]. Trafficking events require the generation of highly curved membrane carriers, that is, small vesicles or narrow tubules protruding into the cytosol. BAR (including N-BARs with N-terminal amphipathic helices) and F-BAR domains generally form homodimers with an intrinsically curved concave membrane-binding interface with which they contribute to the formation of trafficking vesicles or tubules[2,3]. They are recruited to the neck of budding vesicles and control the later recruitment of proteins such as dynamin[4]; they also assemble into scaffolds to deform membranes, for instance in yeast[5]. Their sensor/bending behaviour depends on their density on the membrane[6], which varies according to cell type.

Unique among the members of the BAR domain superfamily, inverted-BAR (I-BAR) domain dimers possess a convex membrane-binding interface. They have a strong structural similarity to BAR and F-BAR domains[7], being elongated dimers with each monomer made up of a three-helix bundle, although their overall shape is markedly flatter than BARs (refs 2,3). Consistent with the convex geometry of their membrane-binding interface, they generate membrane invaginations when bound to the outer leaflet of artificial liposomes[8–10]. In contrast, BAR and F-BAR generate membrane protrusions in similar assays[11]. However, the curvature generated by I-BAR and F-BAR domain proteins is shallow in general (tubule diameter 40–60 nm)[8,12], whereas BAR and N-BAR domains produce much more pronounced bending (tubule diameter ~20 nm)[13,14]. It is not clear yet if this structural difference may lead to functional differences.

IRSp53 (Insulin Receptor tyrosine kinase Substrate Protein of 53 kDa) is the best-studied member of the I-BAR family. It has a modular structure, comprising the N-terminal I-BAR domain, a partial CRIB motif (Cdc42/Rac-interactive binding motif), which binds the small GTPase Cdc42, and an SH3 domain, which recruits a number of regulators of actin polymerization (such as vasodilator-stimulated phosphoprotein (VASP) (ref. 15), Mena (ref. 16), Eps8 (ref. 17), mDia1 and WASP-family verprolin-homologous protein 2 (WAVE2) (ref. 18))[19,20]. IRSp53 also binds to the plasma membrane through its I-BAR domain, and thus constitutes a functional platform at the interface between the plasma membrane and the actin cytoskeleton[21]. Together with its binding partners[15–18], it is involved in the Cdc42-dependent formation of filopodia, which are finger-like membrane protrusions containing actin bundles[22] with a diameter typically ranging between 100 nm and a few hundred nm (ref. 23). Filopodia formation is impaired on IRSp53 inhibition[15]. Overexpression of the I-BAR domain results in the formation of plasma membrane protrusions[8,10,24], which are uncoupled from bundled actin filaments[21,25]. This suggests that at high-density I-BAR domains can scaffold cell membranes. When the full-length protein is expressed at endogenous level, IRSp53 clusters have been observed at the plasma membrane preceding further recruitment of actin regulators and filopodia extension[15]. Nevertheless, the mechanism behind filopodia initiation involving IRSp53 spatial localization remains obscure. For example, whether I-BAR domains can sense negative membrane curvature through their convex geometry has not been examined. In the case of N-BAR domain proteins, systematic biophysical studies have characterized the reciprocal relation between membrane curvature and protein density[26,27]. A similar approach would help in deciphering the *in vivo* function of the I-BAR domain of IRSp53, but does not yet exist[15].

To address how IRSp53 couples to membrane curvature, we used an *in vitro* system that has largely been exploited to study the effect of curvature on lipid[28,29] and protein sorting[26,27,30,31]. By pulling membrane tubes of controlled radius from giant unilamellar vesicles (GUV; Fig. 1), and using confocal fluorescence microscopy, we are able to measure curvature-induced sorting of the I-BAR domain. This set-up further enables us to record changes in the mechanical properties of the system that occur on binding of the protein to the membrane. To mimic the cellular localization of the protein with respect to curved membranes (facing the interior of membrane tubules), a new method of encapsulation was developed, which does not require the use of hydrophobic solvents that contaminate the membrane bilayer[32].

In this study, we combine experiments with a general theoretical description to investigate the coupling between negative membrane curvature and I-BAR domain density. We find that protein sorting depends non-monotonically on tube curvature, with an optimum value at an intrinsic curvature associated with the protein, $\bar{C}_p$. Our experiments and model also point to the capacity of these proteins to scaffold membranes at moderate density on the flat membrane. Strikingly, we discover that protein-decorated tubes may undergo phase separation into coexisting domains of different curvatures. Our work shows that this results from a mechanical coupling between the shallow I-BAR and the curved tube, independently of direct interactions between proteins. This phase separation might have implications for the role of IRSp53 in the generation of filopodia.

Results

IRSp53 I-BAR is enriched on negatively curved membranes. It was previously shown[8] that the I-BAR domain of IRSp53 efficiently binds liposomes containing the negatively charged lipid L-α phosphatidylinositol-4,5-bisphosphate (PI(4,5)P$_2$), the most abundant phosphoinositol in the cytosolic leaflet of the plasma membrane[33]. Here we use GUVs containing 8% PI(4,5)P$_2$ (mol mol^{-1}), supplemented with 10% 1,2-dioleoyl-sn-glycero-3-phospho-L-serine (DOPS). This lipid composition guarantees binding of the I-BAR domain to the membrane, and was used throughout the study. A small fraction of a lipidated dye (BodipyTR Cer, red-emitting) was incorporated in the lipid mixture, enabling to detect the membrane with confocal fluorescence microscopy. The I-BAR domain was labelled with Alexa 488 (green-emitting dye) and was detected in a separate channel.

To measure potential protein enrichment due to membrane curvature, we pulled membrane nanotubes from GUVs. Briefly, a single GUV is aspirated in a micropipette, with the adjustable pressure difference between the interior of the pipette and the experiment chamber setting the membrane tension of the GUV. A micron-sized bead trapped in an optical tweezers is then used to mechanically pull the membrane nanotube[26,31]. The radius of the nanotube R is directly set by the membrane tension σ : $R = \sqrt{\frac{\kappa}{2\sigma}}$ with κ the bending rigidity of the membrane. R typically ranges from ~7 to 100 nm in the case of bare nanotubes (that is, in the absence of proteins bound to the tubes). Our system thus consists of a large membrane reservoir with a quasi-zero curvature connected to a highly curved membrane tube, making it ideal to study curvature-induced protein sorting[6].

From its structure and its ability to induce membrane deformations with a negative curvature[8], we hypothesized that IRSp53 may have a high affinity for negatively curved membranes, and conversely a very low affinity for positively curved membranes. Here the curvature of the membrane C is defined as being positive if the membrane is locally bent towards the protein solution, and negative if it is bent away.
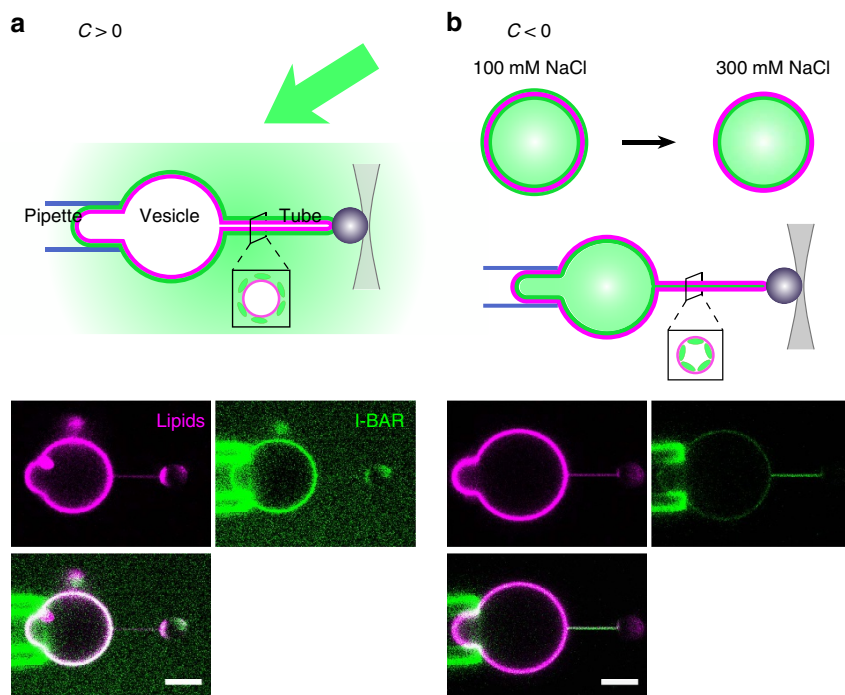
Figure 1 | IRSp53 I-BAR dimers have a strong preference for negative membrane curvature. (**a**) Interaction of the I-BAR with positive membrane curvature. Top: A single GUV is aspirated in a micropipette (blue lines), which allows controlling its membrane tension. A bead (grey sphere) trapped in an optical tweezers (grey beam) is used to pull a membrane nanotube from the GUV. The protein is injected outside the GUV (green arrow), and therefore interacts with the positively curved outer leaflet of the tube (box). Bottom: representative confocal microscopy image. (Note that green fluorescence on the pipette results from adhesion of free protein to the glass.) Scale bar, 5 µm. (**b**) Interaction of the I-BAR with negative membrane curvature. Top: GUVs are grown in the presence of IRSp53 I-BAR dimers in 100 mM NaCl. The protein binds to both the inner and outer leaflets of GUVs. The vesicles are then transferred into a 300 mM buffer, driving the detachment of most of the proteins bound to the outer leaflet. A tube is then pulled from the GUV as in **a**. In this assay, the protein interacts with the negatively curved inner leaflet of the nanotube (box). Bottom: representative confocal image. Scale bar, 5 µm.

For a tube, membrane curvature is thus positive for a protein binding to the external leaflet, and negative for a protein binding to the internal leaflet (see sketches of the tube cross-section at the top of Fig. 1a,b, respectively). Following an established protocol[26,34], we first checked the absence of protein enrichment on positively curved membranes: we pulled membrane tubes from GUVs, and subsequently micro-perfused the protein near the GUVs (Fig. 1a, top). We found that the fluorescence signal of the protein on the tube was very weak, suggesting that the I-BAR domain indeed has a low affinity for positive curvature (Fig. 1a, bottom).

With the tube-pulling experiment, it is in principle possible to study the affinity of proteins for negative curvature, provided that these proteins are present inside the GUV. Different methods have been reported for protein encapsulation in GUVs, either using transfer of inverted emulsion droplets covered with a lipid monolayer through a second monolayer at an oil–water interface[35–38], jetting of a protein solution through a black lipid film[39], or spontaneous GUV swelling on a polymer gel[40,41]. Although the first method appears promising, oil residues are trapped in the bilayer during the passage through the interface, compromising the mechanical properties of the membrane[32]. The two other methods are not suitable as well, because of oil present in black films and the large fraction of multilamellar vesicles, respectively. We thus designed a new assay to encapsulate the I-BAR domain inside unilamellar giant liposomes with controlled mechanical properties. We used an electroformation technique that was developed to enable the production of GUVs in buffers containing physiologically relevant salt concentrations[42], in contrast with the original method[43]. We thus grew GUVs in the presence of the protein in an appropriate buffer containing 100 mM NaCl. After this stage, the protein is present both inside and outside the GUVs, and can thus bind symmetrically to both leaflets (Fig. 1b, top).

However, since the I-BAR binds to lipid bilayers mostly through electrostatic interactions[9], screening these interactions should drive net desorption of the protein. Indeed, we verified that GUVs decorated with the I-BAR on their outer leaflet only, displayed almost complete detachment of the protein on transfer to a high-salt (300 mM NaCl) buffer solution. We estimate the residual protein area fraction to be around ~0.5% (Supplementary Fig. 1). Thus, for our tube-pulling experiments, we transfer the freshly prepared GUVs into an external buffer containing 300 mM NaCl, to only retain vesicles containing I-BAR bound to the inner leaflet (Fig. 1b, top). With this method, a good yield of GUVs can easily be obtained, with I-BAR domains asymmetrically bound on the internal leaflet of the GUVs. In our conditions, starting from a bulk concentration of 50–100 nM, we obtained a wide range of protein density on the membrane (from about 100 up to ~1,200 proteins per µm², equivalent to an area fraction of ~1–6%, as can be estimated from the fluorescence of the protein on the GUVs (see Methods section)). This spread might be explained by a non-uniform distribution of $PI(4,5)P_2$ and/or DOPS across the GUV sample obtained by electroformation[44,45]. Nevertheless, we bypass this issue since the protein density is measured individually on each vesicle.

We performed tube-pulling experiments on GUVs with encapsulated IRSp53 I-BAR. As evidenced by fluorescence images (Fig. 1b, bottom), the I-BAR domain is greatly enriched in the tube, demonstrating that it indeed is a sensor of negative membrane curvature. A systematic quantitative assessment of sorting versus curvature is presented hereafter.

Optimal negative curvature for IRSp53 I-BAR sorting. The enrichment of the protein on the tube (relative to its density on the GUV), called here the sorting ratio, is expected to depend on the curvature of the tube. We next systematically investigated this dependence for varying values of the protein area fraction on the GUV, ϕ_v. Note that, because of the residual proteins bound to the external leaflet, we slightly over-estimate ϕ_v in the following.

By definition, the sorting ratio is given by $S = \frac{\phi_t}{\phi_v}$, with ϕ_t being the protein area fraction on the tube[26,31]. Both the sorting ratio and the curvature of the tube can be calculated based on fluorescence measurements: S corresponds to the ratio of the fluorescence intensity of the protein on the tube I_t^p and on the GUV I_v^p, normalized by the same ratio for the lipid fluorescence: $S = \frac{I_t^p/I_v^p}{I_t^l/I_v^l}$; the radius of the tube R (the inverse of the membrane curvature C) is proportional to the ratio of the fluorescence of the lipids in the tube and in the GUV[26] (see Methods section for more details).

In a typical experiment, fluorescence and force data were collected on a stepwise increase of membrane tension (which corresponds to a stepwise decrease of tube radius). Usually these steps were then reversed, to ensure that our measurements reflected thermodynamic equilibrium (which should result in overlapping curves). We present here the data obtained in the first part of each experiment. The data obtained in the second part are shown in Supplementary Fig. 2.

Each experiment yields, for a fixed value of ϕ_v, the values of the sorting ratio corresponding to different curvatures. Previous measurements of curvature-induced sorting of different proteins[26,27,31,46] have shown that the sorting ratio at a given curvature generally depends on ϕ_v. We therefore binned our fluorescence measurements into three ranges of ϕ_v (more details can be found in Methods section). Fig. 2a shows representative images for GUVs with ϕ_v in each range. Interestingly we found that the sorting curves display a non-monotonic shape. This feature is most striking at the lowest densities ($\phi_v \sim 1\%$), with a maximum of sorting for $C \approx 0.055$ nm^{-1}, that is, $R \approx 18$ nm (Fig. 2b, magenta points). Thus, at very low density, the I-BAR

domain of IRSp53 is highly curvature-selective. The sorting effect is quite strong, since the I-BAR domain is enriched in the tube by a factor of up to ~ 20. Interestingly, the curvature-selectivity is less pronounced when the protein is bound at a higher density on the GUV membrane: the relative enrichment becomes weaker and less peaked for $\phi_v \sim 2$ and 5% (Fig. 2b, green and cyan points, respectively), although sorting remains significant, of the order of 4–5 at $\phi_v \sim 5\%$. We note, however, that the absolute protein density on the tube, ϕ_t, does increase with increasing ϕ_v; see Supplementary Fig. 3.

For comparison, we show on the same graph our data of sorting on tubes with positive curvature. The sorting ratio is between 0 and 1 for the range of curvature investigated, implying that the I-BAR domain does not have any preference for positive membrane curvature (Fig. 2b, grey points).

The dependence of IRSp53 sorting on tube curvature can be understood by thermodynamic arguments, accounting for the membrane bending and stretching energies, the protein mixing entropy, and the energetic coupling between protein and membrane[47,48]. Putting these elements together, the free energy of the tube decorated with proteins with area fraction ϕ_t is given by:

$$F_t = 2\pi R L \left[\frac{\kappa}{2R^2} + \frac{\bar{\kappa}}{2}\phi_t \left(\frac{1}{R} - \left| \bar{C}_p \right| \right)^2 + f_s + f_m \right], \quad (1)$$

where L is the tube length, $\bar{\kappa}$ is an elastic coefficient penalizing mismatch between protein and membrane curvatures and $\left| \bar{C}_p \right|$ is the membrane-bound protein's intrinsic curvature. Also, f_s and f_m are the membrane stretching and mixing energy densities, and depend on the protein and lipid densities; a particular model choice for these densities is specified in Supplementary Note 1. We note that the above protein-membrane coupling term is generic and based on symmetry, and a similar term has been used in other contexts[49,50]. In the absence of any other free energy penalties, the energy of a protein-membrane patch is minimum if the protein and membrane curvatures, $1/R$ and $\left| \bar{C}_p \right|$, match; to lowest order, the energy is quadratic in their difference. The mixing energy refers to the entropy of mixing of a model two-
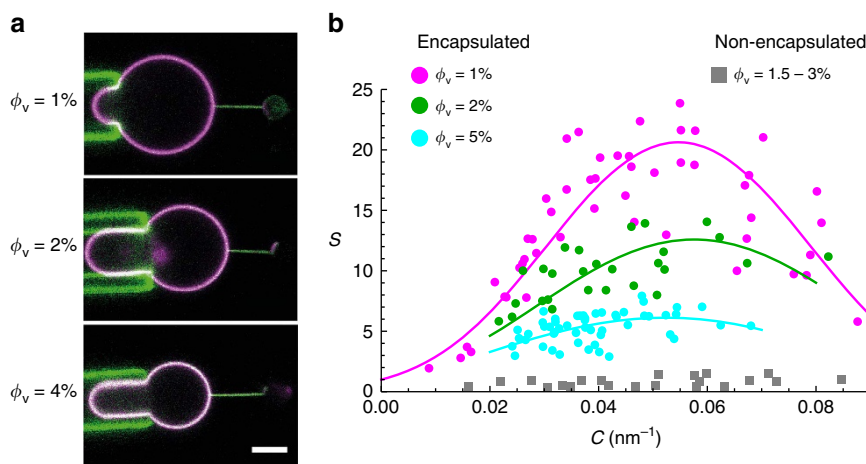

Figure 2 | Quantification of I-BAR enrichment on highly curved membranes. (**a**) Representative confocal images at similar tensions. Top: $\sigma_v = 0.11$ mN m^{-1}. The tube curvature is $C = 0.04$ nm^{-1}. Middle: $\sigma_v = 0.27$ mN m^{-1} ($C = 0.05$ nm^{-1}). Bottom: $\sigma_v = 0.09$ mN m^{-1} ($C = 0.03$ nm^{-1}). (**b**) Sorting ratio, S, as a function of tube curvature, $C = 1/R$, in the case where the protein interacts with positive (squares) and negative (circles) membrane curvature. For negative curvature, three conditions of protein area fraction ϕ_v on the GUVs were investigated (see Methods section): $\phi_v \approx 1\%$ (magenta, $N = 9$ GUVs), $\phi_v \approx 2\%$ (green, $N = 5$ GUVs) and $\phi_v \approx 5\%$ (cyan, $N = 10$ GUVs). A fit to the three data sets using equation (2) yields an average protein intrinsic curvature, $\left| \bar{C}_p \right| = (0.055 \pm 0.003)$ nm^{-1}, and an average protein-membrane elastic parameter, $\bar{\kappa} = (35 \pm 7) k_B T$. For positive curvature (grey), the protein area fraction on the GUVs was in the range 1.5–3% ($N = 4$ GUVs). Scale bar, 5 µm.

component membrane consisting of I-BAR proteins and lipids. By requiring that the lipid and protein chemical potentials on the vesicle and on the tube are equal at equilibrium (Supplementary Note 1), we obtain an implicit dependence of ϕ_t on the curvature:

$$\frac{\phi_t}{\phi_v}\left(\frac{1-\phi_v}{1-\phi_t}\right)^{a_p/a_l} = \exp\left[\frac{\bar{\kappa}a_p}{k_B T}\left(\frac{|\bar{C}_p|}{R} - \frac{1}{2R^2}\right)\right], \quad (2)$$

where a_p and a_l are the protein and lipid areas, respectively. At low densities, ϕ_v and $\phi_t \ll 1$, the quantity in brackets on the left side of equation (2) tends to one, and thus the sorting $S = \phi_t/\phi_v$ has a Gaussian dependence on tube curvature $C = -1/R$, with a maximum at $C = -|\bar{C}_p|$. We note that equation (2) predicts that S decreases with increasing ϕ_v, in agreement with the above experimental data (Fig. 2b). Indeed, when ϕ_v increases, keeping all other parameters equal, the tube area fraction ϕ_t ultimately saturates, and thus grows more slowly than linearly with ϕ_v.

The sorting data for IRSp53 are fitted using equation (2), with $\bar{\kappa}$ and $|\bar{C}_p|$ as free parameters. The ratio $\gamma = a_p/a_l$ is, in principle, a free parameter, though does not have a strong effect on the sorting or on the mechanical effects of proteins on the tube for $\phi_v \ll 1$ (γ appears in logarithmic terms in mixing energy); see Supplementary Note 1. For simplicity of analysis, we assume throughout $\gamma = 1$. We therefore fit the sorting data in the three different vesicle density regimes, $\phi_v = 1$, 2 and 5%, (Fig. 2b), obtaining for the intrinsic curvature, $|\bar{C}_p| = (0.055 \pm 0.003)\,\text{nm}^{-1}$ $(1/|\bar{C}_p| \approx 18\,\text{nm}$, averaged over the three density ranges. In addition, we find $\bar{\kappa} \approx (35 \pm 7)k_B T$. We note finally that the low value that we find for $|\bar{C}_p|$, as compared with the N-BAR protein, Amphiphysin 1 (ref. 26), is fully consistent with the known, shallow shape of IRSp53 (ref. 7).

IRSp53 I-BAR reduces the force needed to sustain the tube. It has been shown that IRSp53 I-BAR, on binding to the outside of lipid vesicles, spontaneously forms invaginated tubes[8]. Accordingly, we found that membrane tubes spontaneously evaginate from GUVs encapsulating the I-BAR, when it is bound at sufficiently high protein coverage (see one example in Supplementary Fig. 4). Thus we expect that bound protein reduces the force, f, needed to hold a pre-formed membrane tube, which is a measurable parameter in our system. It can indeed be deduced from the displacement of the bead within the trap (see Methods section for more details). For bare membranes, f is

related to the membrane-bending rigidity κ and the pipette-controlled tension σ_v (ref. 51) via $f \approx f_0 + 2\pi\sqrt{2\kappa\sigma_v}$, where f_0 is a force offset (it takes into account effects, such as the imperfect passivation of the pipette, which could result in some degree of adhesion of the membrane to the glass, affecting membrane tension). Performing tube-pulling experiments on protein-free GUVs as a control, we obtained $\kappa \approx 12.5\,k_B T$, and $f_0 \approx 5\,\text{pN}$ (Supplementary Fig. 5a).

We then measured the pulling force in the presence of I-BAR. We observed that, for given σ_v, f steadily decreases with respect to the bare membrane reference as the protein density ϕ_v increases; see Fig. 3a. These measurements indicate that, with increasing ϕ_v, proteins have a greater mechanical effect on the curved membrane and, in fact, stabilize the tube. This effect is seen very clearly at $\phi_v \sim 5\%$ and at low membrane tension: in these conditions, the tube becomes floppy, indicating that the pulling force is zero (see Supplementary Fig. 2b, lower inset).

In the presence of proteins, the tube force, as a function of applied tension, is calculated by minimizing the free energy, equation (1), with respect to tube length, L, at fixed radius and at fixed lipid and protein number; see Supplementary Note 1. In this calculation, ϕ_t is given by its equilibrium expression and the tube radius by the value that satisfies radial force balance on a tube element; see below and Supplementary Note 1. As a result, the dependence of f on σ_v is non-trivial, and must in general be found numerically. In this way, the force data are fitted for the three values of ϕ_v, yielding $\bar{\kappa} \approx (32 \pm 12)k_B T$; see Fig. 3a. As expected, for a given σ the force shifts downwards as ϕ_v increases, indicating a stabilizing influence of the proteins.

We can understand the dependence of f on ϕ_v more naturally if we assume that $1/R \lesssim |\bar{C}_p|$, ϕ_v is not negligible but still much $\ll 1$, and $\bar{\kappa}\,a_p|\bar{C}_p|^2/(k_B T) \gg 1$ (so that the tube is nearly saturated with proteins). We then obtain

$$f \approx f_0 - 2\pi\bar{\kappa}|\bar{C}_p| + 2\pi\sqrt{2(\bar{\kappa}+\kappa)\left(\sigma_v - \frac{k_B T}{a_p}\ln \phi_v\right)} \quad (3)$$

where $a_p \approx 50\,\text{nm}^2$ is the area per protein[7].

From this equation we note that f decreases with increasing ϕ_v, in agreement with our data. In addition, taking the values $\bar{\kappa} \approx 40k_B T$ and $|\bar{C}_p| \approx 0.05\,\text{nm}^{-1}$ obtained from the sorting fits, we find the offset term $f_0 - 2\pi\bar{\kappa}|\bar{C}_p| < 0$ As a result, from equation (3) it is clearly seen that the force vanishes at a non-zero
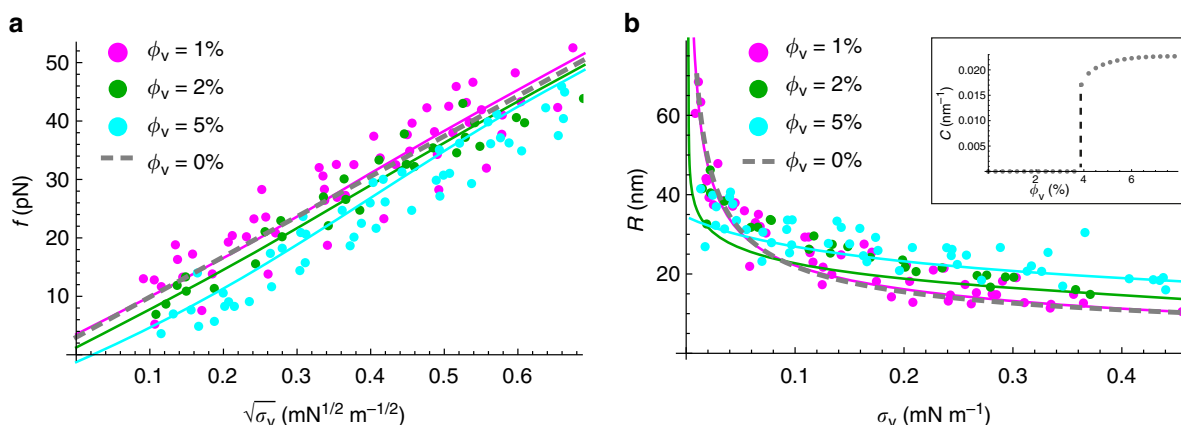

Figure 3 | Mechanical effect of I-BAR binding to the inner leaflet of membrane tubes. (**a**) Pulling force, f, as a function of the square root of tension, $\sqrt{\sigma_v}$, for three different values of ϕ_v : 1% (magenta, $N = 9$ GUVs), 2% (green, $N = 5$ GUVs) and 5% (cyan, $N = 10$ GUVs). Fitting yields (see Supplementary Note 1 for details) an average value of the protein-membrane elastic parameter $\bar{\kappa} = (32 \pm 12)\,k_B T$. The dashed line corresponds to a fit to the data obtained for bare GUVs (Supplementary Fig. 5a). (**b**) Tube radius, R, as a function of σ_v, for the same conditions as in (**a**). Fitting yields $\bar{\kappa} = (60 \pm 30)\,k_B T$. The dashed line corresponds to a fit to the data obtained for bare GUVs (Supplementary Fig. 5b). Data and fit for $\phi_v = 5\%$ indicate that R extrapolates to a finite value at zero tension, whereas for $\phi_v = 1$ and 2% it diverges. Inset shows calculated jump in tube curvature ($1/R$) at zero tension as a function of ϕ_v.

tension, that varies as $\ln \phi_v$. Thus, our model predicts that bound IRSp53 can stabilize membrane tubes, without an external pulling force. It is, furthermore, consistent with observations of spontaneous tubulation of membranes by IRSp53.

Tube curvature is set by IRSp53 I-BAR at high density. The dependence of the tube radius on the protein area fraction on the GUV provides a second way to assess the mechanical effects that proteins have on pre-formed, highly curved membrane structures. In the absence of protein, R has a straightforward relationship to GUV membrane tension σ_v: $R = \sqrt{\kappa/2\,\sigma_v}$. This expression is used to fit the data obtained with bare GUVs (Supplementary Fig. 5b). In the presence of protein, we found that the radius, as a function of applied tension, clearly deviates from the bare membrane reference as the protein density increases: for $\phi_v \sim 1\%$, the curve overlaps with the data for bare tubes, indicating negligible mechanical changes to the tube. In contrast, for $\phi_v \sim 2$ and 5%, there is a marked difference between the radii of bare and protein-decorated tubes; see Fig. 3b: (a) the overall dependence of the tube radius on tension is much less pronounced, (b) the coated-tube is wider for most of the range of membrane tension explored and (c) at vanishing tension $\sigma_v \to 0$, the tube curvature tends to a non-zero value.

At mechanical equilibrium the tube radius is found by minimizing the tube free energy, equation (1), with respect to R for fixed L, and lipid and protein number. The result of the minimization yields an equation that depends on the applied tension, σ_v, and the protein area fraction on the tube, ϕ_t, which in turns depends on R. As a result, for a given σ_v, R must generally be found numerically; see Supplementary Note 1 for details. The experimental values of R versus σ_v for given ϕ_v can be fitted with the above-described theory with $|\bar{C}_P|$ and $\bar{\kappa}$ as unknown parameters in principle ($\gamma = a_p/a_l$ is fixed equal to 1 as mentioned before). Since the value of $|\bar{C}_P|$ obtained from the sorting fits across the three density regimes was constant to within $<10\%$, we subsequently assumed $|\bar{C}_P| = 0.052\,\mathrm{nm}^{-1}$. Fitting the data, we obtain $\bar{\kappa} \approx (60 \pm 30)k_BT$.

From the tube radius fits we find that the model captures well the observed mechanical effects of bound IRSp53. First, the fits confirm that at moderately high protein densities ($\phi_v \sim 5\%$) and at large tension ($\sigma_v \gtrsim 0.1\,\mathrm{mN\,m}^{-1}$), tubes are wider than they are for bare membranes; see Fig. 3b. This feature is, on first inspection, surprising given that proteins stabilize membrane tubes, and one would expect they favour higher curvatures than that of a bare case. This behaviour can, however, be understood from an approximate expression for R, valid under the same assumptions leading to equation (3):

$$R \approx \sqrt{\frac{\bar{\kappa} + \kappa}{2\left(\sigma_v + \frac{k_BT}{a_p}\ln(1/\phi_v)\right)}} \qquad (4)$$

Equation (4) resembles the expression for the bare tube radius, $R \approx \sqrt{\kappa/2\sigma_v}$, but shows that the protein-decorated tube radius increases with increasing ϕ_v, and that the effective rigidity is higher, given by $\kappa + \bar{\kappa}$. We note that in this regime, R is neither strongly dependent on applied membrane tension, nor is it fixed by the intrinsic curvature $|\bar{C}_P|$. In fact, for $\phi_v = 5\%$ and $a_p \approx 50\,\mathrm{nm}^2$, the entropic part of the tube tension is $\frac{k_BT}{a_p}\ln(1/\phi_v) \approx 0.25\,\mathrm{mN\,m}^{-1}$, and therefore for most of the tensions explored $R \approx \sqrt{\frac{\bar{\kappa} + \kappa}{2\frac{k_BT}{a_p}\ln(1/\phi_v)}} \approx 20\,\mathrm{nm}$, assuming $\kappa = 15k_BT$ and $\bar{\kappa} = 40\,k_BT$, in agreement with Fig. 3b.

Second, our model confirms that at vanishing applied tension and the highest protein density ($\phi_v \approx 5\%$) the tube curvature

tends to a finite value, whereas at low densities it tends to zero, just as for a protein-free tube (Fig. 3b). By calculating the tube curvature at zero tension as a function of ϕ_v, we see that there is a discontinuous change in the curvature at a given $\phi_v \approx \frac{\kappa}{\bar{\kappa}}\left(\frac{k_BT}{a_p\bar{\kappa}|\bar{C}_P|^2}\right)$; see inset of Fig. 3b and Supplementary Note 1. This provides further quantitative proof that IRSp53 can stabilize tubes, depending on their intrinsic curvature, and consistent with their ability to tubulate flat membranes. Indeed, if a sufficient quantity of protein is bound to a floppy vesicle, highly curved structures are energetically favoured over nearly flat membrane. Finally, the discontinuous nature of curvature at vanishing tension is indicative of bistability, pointing to the possibility of coexisting phases on the tube at low tension.

IRSp53 I-BAR phase separates on the tube. We have shown so far that encapsulated IRSp53 is enriched on membrane tubes with a uniform coating of the tubes (Fig. 1b). Interestingly, at low applied tensions ($\sigma_v \lesssim 0.01\,\mathrm{mN\,m}^{-1}$) and at vesicle protein densities between 1 and 2%, we observed coexistence of two phases along the tube, with different protein densities and different radii (Fig. 4a). The protein-rich part of the tube (green in Fig. 4a) was found to have a much smaller radius than the nearly bare part (magenta).

We consistently observed protein phase separation along the tube for low tensions and low protein densities, as shown in Fig. 4b (filled circles). In cases where it was observed, phase separation was detected at the first image acquisition, typically about 1 min after a change in membrane tension; no further evolution was detected on subsequent imaging (for 1–3 min). Although in general phase separation was obtained following a stepwise decrease of membrane tension, it was also observed when ramping up from low tension (filled triangle in Fig. 4b and Supplementary Fig. 6.

We measured tube radii between 30 and 40 nm for the protein-coated part, and >70 nm for the protein-depleted one (Fig. 4c). In addition, for a subset of conditions, we observed that the lipid and protein fluorescence along the tube was inhomogeneous, yet there were not two clearly distinct domains (grey squares in Fig. 4b. See an example in Supplementary Fig. 7). This suggests incomplete phase separation, at least on the timescale (maximum 5 min) of our experiment.

Strikingly, we also found IRSp53 clustering *in vivo* which is consistent with the ability of I-BAR domain proteins to phase separate *in vitro*. Live-cell imaging experiments on U2OS cells expressing GFP-fusion of full-length IRSp53 revealed that filopodia formation was often preceded by formation of an IRSp53 cluster at the membrane. We note that similar clustering of I-BAR domain proteins IRSp53 and missing-in-metastasis (MIM) has also been reported before filopodia elongation in mouse embryonic fibroblasts and in rat primary neurons[15,52]. Importantly, the clustering of IRSp53 appears to be independent of actin polymerization. This is because also the isolated I-BAR domain of IRSp53, which lacks the regions required for interactions with G-actin and regulators of actin dynamics such as cdc42, VASP and Eps8 (ref. 22), is able to form clusters at the plasma membrane before the elongation of the filopodium (Supplementary Fig. 8).

Interestingly, phase separation along the tube is predicted by our model for low tensions. Briefly, it occurs because of the non-linear interaction between the density of curved proteins and tube curvature, as contained in the energy, equation (1). In fact, for a certain range of ϕ_v and at low tension, the tube radius is a multi-valued function of σ_v (Supplementary Note 1): one solution
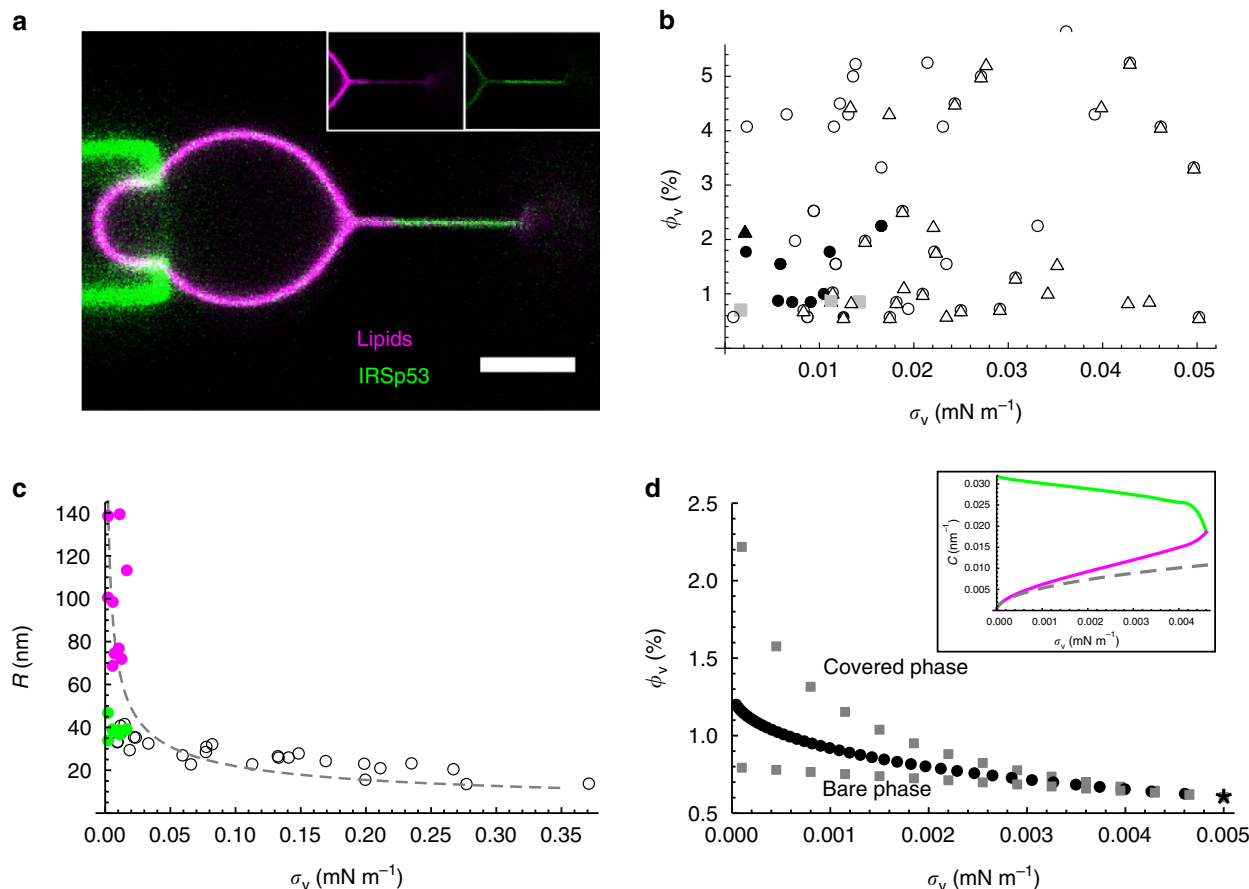
Figure 4 | Phase separation along the tube at low membrane tension. (**a**) Confocal image showing the coexistence of two phase of the tube: a wide, protein-poor phase (magenta) and a narrow, protein-covered one (green). The inset shows the separate channels. Here $\phi_v \sim 2\%$ and $\sigma_v \approx 0.017\,\text{mN m}^{-1}$. Scale bar, 5 μm. (**b**) Phase diagram in the $\phi_v - \sigma_v$ plane. Filled circles (triangle) indicate phase-separated tubes observed while decreasing (increasing) tension. Open circles (triangles) indicate single-phase tubes observed while decreasing (increasing) tension. Grey squares indicate incompletely phase-separated tubes observed while decreasing tension. $N = 32$ GUVs. (**c**) Tube radius, R, versus tension, σ_v. Open circles indicate single-phase tubes (for $\phi_v \sim 2\%$, $N = 5$ GUVs). Magenta and green filled circles indicate radii of protein-poor and protein-covered coexisting phases, $N = 8$ GUVs. The fit to the data for bare GUVs, indicated by a dashed line, is provided as a reference. (**d**) Theoretical $\phi_v - \sigma_v$ phase diagram. Points at which nearly bare and protein-covered phases coexist are indicated by filled circles. The limits of metastability are indicated by grey squares (upper set: limit of bare phase; lower set: limit of covered phase). The predicted critical point is indicated by an asterisk. Inset shows the curvatures of phases at coexistence (same colour code as in **c**); dashed line is analytical approximation to bare phase curvature, as obtained from Supplementary Equation 33. The model parameter values are $\bar{\kappa} = 24\,k_BT$, $|\bar{C}_p| = 0.055\,\text{nm}^{-1}$, $\bar{\kappa} = 70\,k_BT$, $a_p = a_l = 50\,\text{nm}^2$ and $\chi = 0$ (direct protein–protein interaction parameter; see Supplementary Equation 5).

corresponds to a bare-like tube (b) in which the curvature tends to zero for vanishing tension, while the second solution (the 'covered phase', c) has a finite curvature for zero tension. For the b and c phases to coexist, the axial forces in the two phases b and c, assumed to be cylindrical, must be equal and the radial forces must balance:

$$f_b = f_c; \frac{\partial F_{tb}}{\partial R_b} = 0; \quad \frac{\partial F_{tc}}{\partial R_c} = 0 \qquad (5)$$

In the above, the derivative is done at constant length, lipid and protein number for a tubular domain. Solving equation (5) numerically yields the unknowns R_b, R_c and the coexistence curve $\phi_v(\sigma_v)$ across which a first order-type transition takes place; see Fig. 4d. Whereas $1/R_b$ approximately follows the $\sigma_v^{-1/2}$ dependence of bare tubes, $1/R_c$ weakly depends on tension, suggesting a scaffold-like protein arrangement; see inset of Fig. 4d. This predicted tension dependence of the two phases agrees qualitatively with the measurements shown in Fig. 4c.

Our model predicts that b and c domains coexist at equilibrium along the $\phi_v(\sigma_v)$ curve, as shown in Fig. 4d. However, metastable pure b or c phases occur off this curve; a thermal fluctuation may trigger nucleation of the other phase, and the resulting dynamics may be very slow in the tubular geometry. The cases of incomplete phase separation (grey squares in Fig. 4b) may be metastable states that are not completely equilibrated. The limits of metastability (spinodal curves), which can be obtained from our model (see Supplementary Note 1 for details), thus confirms that there is a window in the $\phi_v - \sigma_v$ phase diagram in which phase-separated tubes may be observed; see Fig. 4d. The coexistence and spinodal curves converge and terminate at a critical point, shown as an asterisk (*) in Fig. 4d.

Thus, we find from our model that distinct phases, with sharply contrasting protein densities and tube radii, can coexist at low tensions and relatively low reservoir protein density, in agreement with our experimental results. Remarkably, the phase separation we have described depends only on the non-linear relation between membrane curvature and protein density, and not on any presumed direct interactions between the proteins themselves.

Discussion

In this work, we have designed an original assay that allows studying binding of proteins on the 'cytosolic' inner leaflet of a GUV. The vesicles obtained through this method are free of oil residues inserted within their lipid bilayer. This technique can be extended in principle to other proteins that bind to membranes essentially through electrostatic interactions. By pulling tubes from GUVs encapsulating proteins, we could measure, for the first time, the preferential binding of proteins on highly negatively curved membranes as well as the membrane deformations they induce. With this assay, we have demonstrated the strong coupling between the I-BAR domain of IRSp53 and negative membrane curvature. We have developed a general theoretical model that reproduces well the ensemble of our data, namely curvature sensing, the effect of I-BAR binding on the tube radius and on the tube force, and phase separation along the tube. Our model contains only two protein-membrane parameters, the intrinsic curvature of the protein $|\bar{C}_p|$ and the elastic constant $\bar{\kappa}$. In contrast with former models, no a priori scaffolding is assumed[30] or protein–protein interactions[26,53] included. In principle, this model should apply to any protein that induces membrane spontaneous curvature; it can be adapted to include interactions that become significant at higher densities. In this respect, this work on IRSp53 provides a representative case study of interactions between curved proteins and curved membranes.

We have shown that IRSp53 I-BAR is maximally sorted at a curvature $1/|\bar{C}_p| \approx 18$ nm. A levelling-off of protein sorting at practically accessible curvature was already reported for a trans-membrane protein[31] with moderate spontaneous curvature $(1/|\bar{C}_p| \approx 25$ nm$)$[31]. In contrast, in the case of N-BAR domain, a maximum was not observed due to their much higher intrinsic curvature (an average of $1/|\bar{C}_p| \approx 3$ nm was found for amphiphysin[26]; simulations found $|\bar{C}_p| \approx 10$ nm for this protein from the membrane curvature that minimizes the binding energy[54]). Despite there being an optimum sorting at around 20 nm, we would still expect a significant curvature-driven protein enrichment in tubular structures, such as filopodia, for diameters of the order of 100 nm.

We found that IRSp53 I-BAR has significant mechanical effects on curved membranes. Even at only 5% protein coverage on the GUV, the tube radius becomes weakly sensitive to the applied tension, suggesting a scaffold-like protein arrangement on the tube[55,56]. Scaffolding by BAR domain proteins was previously attributed to the formation of organized protein coats, connected through either amphipathic helices (in the case of N-BAR domains[56]), or lateral interactions between adjacent BAR domains (in the case of F-BAR domains[55]). However despite its lack of amphipathic helices, and even if bound at non-saturating densities on tubes (maximum 35%), we find that the I-BAR domain of IRSp53 is able to scaffold membranes. This suggests that coupling with membrane curvature might be sufficient to explain scaffolding, in the absence of extensive protein–protein interactions.

We note here that the so-called scaffold radius, deduced from invagination assays and measured with electron microscopy, is not simply given by $1/|\bar{C}_p|$. Nonetheless, this parameter is biologically relevant, as our model predicts that the radius of a spontaneous invagination (formed at zero force) is of the order of, but slightly greater than, $1/|\bar{C}_p|$ (see Supplementary Note 1 and Supplementary Equation 32); indeed, I-BAR-induced invaginations of synthetic liposomes have an average radius of ∼20 nm (ref. 9). Biologically, IRSp53 acts in concert with other proteins and with actin bundles to form and maintain filopodia. Still, its ability to spontaneously evaginate membranes likely facilitates filopodia formation. Indeed, when overexpressed,

IRSp53 can form filopodial structures, even without actin bundles[21,25].

We have also shown here that the strong influence that the I-BAR has on the tube radius is mirrored by the existence of phase separation along the tube. While previously conjectured[53], we report here the first known observation of protein phase separation on membrane tubes. Both experiments and model demonstrate that, at low tension and at low protein density, protein-covered and thin tubular domains (c) coexist with quasi-bare, wide ones (b). The radii of the c domains only weakly depend on tension (Fig. 4c,d), while the b radii follow the $\sigma_v^{-1/2}$ dependence of bare tubes. Interestingly, we found that direct attractive interactions between proteins are not essential for phase separation; here, indirect interactions mediated by the curved membrane tube are sufficient. This is in contrast to ref. 53, in which only direct interactions were considered. Direct interactions, which can be modelled using a mean-field expression of the type $\chi\phi^2$, with $\chi < 0$, only qualitatively shift the phase coexistence line, shown in Fig. 4d; see, also, Supplementary Fig. 9. Experimentally, there is no evidence of direct interactions between IRSp53 proteins leading to phase separation: (i) gel filtration with purified IRSp53 did not reveal any trace of oligomerization, limited amounts of oligomers were detected on a native PAGE gel (Supplementary Fig. 10), and (ii) we never optically detected IRSp53 clusters on the nearly flat GUV. These facts indicate that attractive interactions, in the
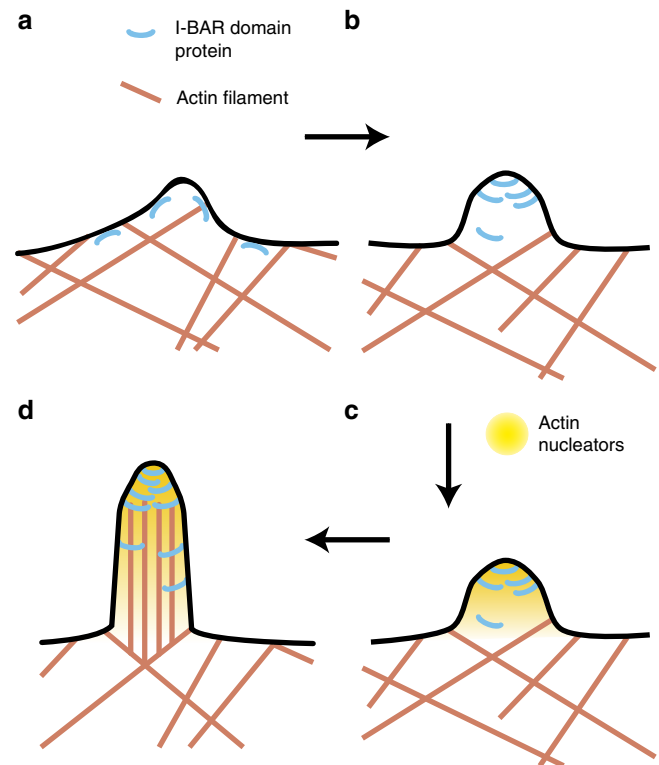

Figure 5 | Proposed model for the role of IRSp53 in the initiation of filopodia. (**a**) I-BAR domain proteins bind to plasma membrane. The protein's intrinsic curvature favours weak negative curvature, which in turn recruits more protein. (**b**) I-BAR domain protein phase separates on curved membrane, forming an I-BAR-rich cluster at the tip of the incipient filopodium. (**c**) The PIP2 patch associated to the I-BAR cluster recruits actin polymerization nucleators. (**d**) Filopodium extension following polymerization of actin. Positive feedback between membrane deformation induced by actin polymerization and actin nucleator recruitment can additionally help filopodium growth.

absence of membrane curvature, are weak. Thus, the non-linear coupling between curvature and protein density embodied in the tube energy provides a robust mechanism for protein aggregation on membranes.

We note that incompletely decorated membrane tubes have also been seen in studies of the GTPase dynamin, which plays a role in severing membrane buds during endocytosis. In that case, however, partial coverage occurs by nucleation and growth eventually leading to the full coverage of the tube[30]. Interestingly, phase separation was not observed in a recent *in vitro* study on the N-BAR protein Amphiphysin 1 (ref. 26). The way this protein interacts with curved membranes appears similar to IRSp53; however, Amphiphysin 1 has a much greater intrinsic curvature $\left[|\bar{C}_\mathrm{P}| = 1/(3\,\mathrm{nm})\right]$, which would explain why the region of the $(\phi_\mathrm{v}, \sigma_\mathrm{v})$ diagram where coexistence can occur is non-observable. Indeed, the value of the GUV protein density at the critical point in the $(\phi_\mathrm{v}, \sigma_\mathrm{v})$ space is approximately given by $\phi_\mathrm{v}^* \sim \exp(-\frac{a_\mathrm{p}\bar{\kappa}|\bar{C}_\mathrm{P}|^2}{k_\mathrm{B}T})$; see Supplementary Note 1. Taking $a_\mathrm{p} = 50\,\mathrm{nm}^2$, $\bar{\kappa} = 40\,k_\mathrm{B}T$ and $|\bar{C}_\mathrm{P}| = 1/(3\,\mathrm{nm})$, the exponential factor is completely negligible. Thus, it appears that a shallow intrinsic protein curvature is essential to observe phase separation.

We can thus propose a new mechanism for the initiation by IRSp53 of plasma membrane protrusions such as filopodia (Fig. 5). At endogenous level, active IRSp53 appears to be present at low density at the plasma membrane[15,21]. It was shown by Disanza *et al.*[15] that IRSp53 forms small clusters about 1 s before recruitment of VASP at the same spot, followed by filopodium growth at the same location a few seconds later. We have also shown here that filopodia formation is often preceded by clustering of a membrane-bound IRSp53, and concomitant curving of the underlying membrane. Similar clustering was recently also reported for full-length MIM (ref. 52), suggesting that this may be a general feature of I-BAR domain proteins. Based on the ability of the I-BAR domain to be locally enriched and constrict a weakly curved membrane, a local and transient fluctuation of the membrane produced by the cytoskeleton could be stabilized and amplified[64] through a phase separation process. The IRSp53 cluster at the tip of the deformation is expected to produce a PI(4,5)P2-rich domain[57,58] that helps recruiting Cdc42; it also gathers actin-related proteins such as VASP, which eventually leads to the growth of filopodia[20]. The shallow curvature of the I-BAR domain is essential for this clustering to occur. Since this phase separation process is general, we could expect that it is also used by other shallow BAR domain proteins that are present at low level at the plasma membrane. This might shed light on the role of F-BAR proteins in the formation of filopodia-like structures *in vitro*[59] and in the initiation *in vivo* of clathrin coats or of dendritic spines in neurons since these events are primed by the clustering of this type of proteins[60,61].

Methods

Reagents. Alexa Fluor 488 C5-Maleimide (Alexa 488), BODIPY TR Ceramide (BODIPY TR), β-BODIPY FL C5-HPC (BODIPY FL) were purchased from Life Technologies. L-α-phosphatidylcholine from chicken egg (egg PC), PI(4,5)P2 from porcine brain, cholesterol from ovine wool, 1,2-dioleoyl-sn-glycero-3-phosphoethanolamine (DOPE), DOPS, 1,2-dioleoyl-sn-glycero-3-phosphocholine (DOPC) and 1,2-distearoyl-sn-glycero-3-phosphoethanolamine-N-(biotinyl (polyethylene glycol)-2,000; DSPE-PEG(2,000) biotin) were purchased from Avanti Polar Lipids. Streptavidin-coated polystyrene particles were from Spherotech. β-Casein (>98% pure) from bovine milk was purchased from Sigma-Aldrich.

Plasmids. The LifeAct-RFP construct was a kind gift from Roland Wedlich-Söldner (Max-Planck Institute of Biochemistry, Martinsried, Germany. Human long isoform IRSp53 was from Japanese Collection of Research Bioresources (JCRB) and cloned into pEGFP-N1 vector (CLONTECH Laboratories, Inc.) by

EcoRI-BamHI sites. GFP fusion of IRSp53 BAR domain was constructed into the XhoI–BamHI sites of pEGFP-N1.

Purification and fluorescent labelling. The IRSp53 I-BAR domain was purified as in ref. 9. For labelling, Alexa 488 C5-Maleimide was dissolved at 20 mM in dimethyl sulphoxide and added at a 1:1 molar ratio to the purified protein. The mixture was kept for 30–60 mn at 4 °C under agitation. Excess dye was removed using a desalting column with 20 mM HEPES pH 7.5, 300 mM NaCl. The concentration of the protein was estimated by measuring the sample absorbance at 280 nm (with a NanoDrop ND 1,000 spectrophotometer, Thermo Scientific), and the labelling efficiency was assessed by measuring the absorbance at 488 nm. The typical labelling efficiency n^* was in the range 1–2 molecules of Alexa 488 per I-BAR dimer. The sample was aliquoted, flash frozen in liquid nitrogen and stored at − 80 °C until use.

Cell culture and transfections. Human osteosarcoma (U2OS) cells (from ATCC) were cultured at + 37 °C in DMEM supplemented with 10% foetal bovine serum (Hyclone), 2 mM L-glutamine, penicillin and streptomycin (Sigma-Aldrich). Transient transfection of U2OS cells was performed with FuGENE HD (Roche) according to manufacturer's instruction. Cells were re-plated on fibronectin-coated (10 µg ml⁻¹ fibronectin) MatTek dishes after 24 h transfection.

Preparation of GUVs. Lipids in powder form were solubilized in chloroform or a mixture of chloroform and methanol to prepare stock solutions. They were subsequently mixed at the following molecular ratio: 57% Egg PC, 8% PI(4,5)P2, 15% cholesterol, 10% DOPS, 10% DOPE, supplemented with 0.1% DSPE-PEG(2000) biotin and 0.5% BODIPY TR (for all experiments except green fluorescence calibration, see below). GUVs were prepared using an electroformation protocol suitable to work with physiological buffers[42]. A few µl of lipid mixture at 3 mg ml⁻¹ were deposited onto platinum electrodes (Goodfellow). The lipid film was dried for at least 30 min. under high vacuum, then rehydrated in one of the following solutions: 200 nM IRSp53 I-BAR in 20 mM Tris pH 7.5, 100 mM NaCl, 350 mM sucrose, 1 mM EDTA and 1 mM EGTA (buffer I1) for the experiments with encapsulated I-BAR; 20 mM Tris pH 7.5, 50 mM NaCl, 150 mM sucrose, 1 mM EDTA and 1 mM EGTA (buffer I2) for experiments with bare GUVs; 20 mM Tris pH 7.5, 100 mM NaCl, 200 mM sucrose, 1 mM EDTA and 1 mM EGTA (buffer I3) for experiments with injected I-BAR. The GUVs were grown overnight at 4 °C under a sine voltage of 0.35 V RMS, 500 Hz.

Tube experiments. Our set-up has been previously described[28]. It comprises a Nikon C1 confocal microscope equipped with optical tweezers and micromanipulators. Micropipettes were used to manipulate individual GUVs and control their tension[62]. The tension is given by $\sigma = \frac{\Delta P R_\mathrm{pip}}{2\left(1 - R_\mathrm{pip}/R_\mathrm{v}\right)}$, where ΔP is the aspiration pressure, R_pip is the pipette radius and R_v is the vesicle radius.

Before the experiment, the chamber was filled with a solution of β-Casein at 5 mg ml⁻¹, to prevent adhesion of the vesicles to the glass surface. The micropipette was back-filled with the same solution before being inserted into the experimental chamber. After a few minutes, the β-Casein solution in the chamber was replaced with the experiment buffer: 20 mM Tris pH 7.5, 300 mM NaCl, 1 mM EDTA and 1 mM EGTA (buffer O1) for the experiments with encapsulated I-BAR; 20 mM Tris pH 7.5, 100 mM NaCl, 50 mM glucose, 1 mM EDTA and 1 mM EGTA (buffer O2) for experiments with bare GUVs; 20 mM Tris pH 7.5, 200 mM NaCl, 1 mM EDTA and 1 mM EGTA (buffer O3) for experiments with injected I-BAR.

A few µl of GUVs and streptavidin-coated beads were then added to the solution. After a few minutes, both edges of the chamber were sealed with mineral oil to maintain a constant pressure inside the chamber. Finally, a GUV was aspirated in the micropipette, and a bead trapped in the optical tweezers. The GUV, held under low tension, was brought into contact with the bead, then moved away to form a membrane tube (thanks to the attachment between biotinylated lipids and streptavidin molecules at the surface of the bead). A few successive step-increases of tension were performed, with 1.5–2 min. equilibration periods. At each step, the position of the bead over time was recorded, and one fluorescence image was acquired (at the end of the 2-min period). When possible, these steps were reversed until reaching a minimal tension again.

Injection. For protein injection, about 1 µl of protein solution at 2 µM was aspirated into the tip of a second micropipette, and then the rest of the pipette was back-filled with mineral oil. This injection pipette was inserted into the side opposite to the first micropipette before closing the chamber. The pipette was kept high enough in the experiment chamber so that the protein would not bind to the GUVs present at the surface of the chamber. Only once a tube was pulled, the pipette was brought close to the GUV, and the measurement was performed as described above. See[26] for more details.

Force measurements. The force was deduced from the displacement of the bead within the trap using the expression: $f = k(x - x_0)$ where k is the trap stiffness, x is the average position of the bead at a given tension and x_0 is its equilibrium position. The position of the bead was measured by video tracking of bright field images

using custom Matlab software. The trap stiffness was measured by the viscous drag method[63].

Image analysis. The system was imaged by fluorescence confocal microscopy in two channels corresponding to the absorption of Alexa 488 and BODIPY TR. On each image, the fluorescence intensities of the GUV and of the tube were measured using custom Matlab software. When performing the experiment, the tube was positioned parallel to the scan lines of the confocal. The fluorescence intensity was subsequently measured as the average fluorescence of the brightest line within a user-defined region of interest (ROI) including the tube. For the GUV, the ROI was positioned such that the part of the GUV analysed would be approximately parallel to the scan lines (with a small deviation due to the curvature of the GUV on confocal sections). The length of the ROI was chosen to be equal to half the radius of the vesicle.

Measurement of tube radius. The values of tube radius given in this article were deduced from the fluorescence intensity of the tube in the lipid (BODIPY TR) channel. The fluorescence intensity was first calibrated as previously described[26,31]. Briefly, for bare GUVs (in the absence of protein bound to the membrane), the radius of the tube can be calculated from the expression: $R_t = \frac{f}{4\pi\sigma}$ (ref. 51), with σ the membrane tension and f the force measured at this tension. On the other hand, the radius is proportional to the amount of fluorophore molecules in the tube, hence to the fluorescence intensity of the tube in the lipid channel I_t^l: $R_t = R_c \frac{I_t^l}{I_v^l}$, where R_c is a constant and I_v^l the fluorescence intensity on the GUV. The normalization is meant to cancel out variations in tube fluorescence due to an uneven distribution of the label among GUVs, or variability in the fraction of the label in the initial mix. This expression holds including when proteins are bound to the membrane. Measurements of force and fluorescence were performed using bare GUVs. The quantity $\frac{f}{4\pi\sigma}$ was plotted against the corresponding value of $\frac{I_t^l}{I_v^l}$ and fitted with a linear function, yielding the calibration constant R_c. We find $R_c = 203 \pm 16$ nm ($N = 11$ GUVs, see Supplementary Fig. 11), in good agreement with previously reported values[26,31].

Measurement of protein density. The density of protein bound to the membrane (number of proteins per unit area) is proportional to the fluorescence intensity in the Alexa 488 channel. The measurement of the calibration factor has also been described in refs 26,31. Briefly, a proportionality constant A was first measured for the lipidated dye BODIPY FL, which can be imaged under the same settings as Alexa 488. This dye was incorporated at several molar ratios in pure DOPC vesicles, and the resulting density of dye molecules was plotted against the fluorescence intensity of the GUVs (40–50 per condition), and fitted with a linear function. A correction factor F accounting for the different spectral characteristics of Alexa 488 and bodipy FL was then measured: bulk solutions of both dyes were imaged, and the correction factor was taken as the ratio of their fluorescence. Finally, the density of protein bound to the membrane was calculated from the formula:$n_v = \frac{A}{Fn^\star} I_v^p$,
where $n^\star$ is the labelling efficiency defined earlier.

The protein surface fraction on the GUV membrane ϕ_v is simply related to its density by: $\phi_v = a_p n_v$,
where a_p is the area of a single protein, $a_p \approx 50$ nm^2 (ref. 7).

Each GUV was characterized by its own protein density, and the full set of data was binned into three ranges of densities:

- Range 1: $140 \leq n_v \leq 23\,\mu m^{-2}$, that is, $0.7 \leq \phi_v \leq 1.15\%$.
- Range 2: $300 \leq n_v \leq 500\,\mu m^{-2}$, that is, $1.5 \leq \phi_v \leq 2.5\%$.
- Range 3: $750 \leq n_v \leq 1250\,\mu m^{-2}$, that is, $3.75 \leq \phi_v \leq 6.25\%$.

Sorting Ratio. The sorting ratio S quantifies the distribution of proteins between the GUV and the tube. It is defined as $S = \frac{I_t^p/I_v^p}{I_t^l/I_v^l}$ where the ratio of green fluorescence in the tube and in the vesicle is normalized by the same ratio for red fluorescence. This is to correct for the difference in membrane areas considered in both measurements (of the tube and of the vesicle). With this definition, $S > 1$ means that the protein is enriched in the tube, and $S < 1$ means that it is depleted from the tube (with respect to its density on the GUV).

Live-cell imaging. Live cells coexpressing IRSp53-GFP full-length protein or isolated BAR domain together with LifeAct-RFP were imaged in 37 °C under a CO2 hood with 3I Marianas (3I intelligent Imaging Innovations). All images were acquired by Zeiss Axio Observer Z1 microsope using a C-Apochromat × 63/1.2 numerical aperture water objective and 488/561 nm solid-state lasers modulated at 50 MHz. 488 s/561 s filters were used for live-cell imaging and images was taken every 2 s. Image analysis was performed using ImageJ software.

References

1. Frost, A., Unger, V. M. & De Camilli, P. The BAR domain superfamily: membrane-molding macromolecules. *Cell* **137,** 191–196 (2009).
2. Suetsugu, S., Toyooka, K. & Senju, Y. Subcellular membrane curvature mediated by the BAR domain superfamily proteins. *Semin. Cell Dev. Biol.* **21,** 340–349 (2010).
3. Mim, C. & Unger, V. M. Membrane curvature and its generation by BAR proteins. *Trends Biochem. Sci.* **37,** 526–533 (2012).
4. Daumke, O., Roux, A. & Haucke, V. BAR domain scaffolds in dynamin-mediated membrane fission. *Cell* **156,** 882–892 (2014).
5. Kishimoto, T. *et al.* Determinants of endocytic membrane geometry, stability, and scission. *Proc. Natl Acad. Sci. USA* **108,** E979–E988 (2011).
6. Callan-Jones, A. & Bassereau, P. Curvature-driven membrane lipid and protein distribution. *Curr. Opin. Solid State Mater. Sci.* **17,** 143–150 (2013).
7. Millard, T. H. *et al.* Structural basis of filopodia formation induced by the IRSp53/MIM homology domain of human IRSp53. *EMBO J.* **24,** 240–250 (2005).
8. Mattila, P. K. *et al.* Missing-in-metastasis and IRSp53 deform PI(4,5)P2-rich membranes by an inverse BAR domain-like mechanism. *J. Cell Biol.* **176,** 953–964 (2007).
9. Saarikangas, J. *et al.* Molecular Mechanisms of membrane deformation by I-BAR domain proteins. *Curr. Biol.* **19,** 95–107 (2009).
10. Suetsugu, S. *et al.* The RAC binding domain/IRSp53-MIM homology domain of IRSp53 induces RAC-dependent membrane deformation. *J. Biol. Chem.* **281,** 35347–35358 (2006).
11. Itoh, T. *et al.* Dynamin and the actin cytoskeleton cooperatively regulate plasma membrane invagination by BAR and F-BAR proteins. *Dev. Cell* **9,** 791–804 (2005).
12. Itoh, T. & De Camilli, P. BAR, F-BAR (EFC) and ENTH/ANTH domains in the regulation of membrane-cytosol interfaces and membrane curvature. *Biochim. Biophys. Acta-Mol. Cell Biol. L* **1761,** 897–912 (2006).
13. Peter, B. J. *et al.* BAR domains as sensors of membrane curvature: the amphiphysin BAR structure. *Science* **303,** 495–499 (2004).
14. Gallop, J. L. *et al.* Mechanism of endophilin N-BAR domain-mediated membrane curvature. *EMBO J.* **25,** 2898–2910 (2006).
15. Disanza, A. *et al.* CDC42 switches IRSp53 from inhibition of actin growth to elongation by clustering of VASP. *EMBO J.* **32,** 2735–2750 (2013).
16. Krugmann, S. *et al.* Cdc42 induces filopodia by promoting the formation of an IRSP53:Mena complex. *Curr. Biol.* **11,** 1645–1655 (2001).
17. Disanza, A. *et al.* Regulation of cell shape by Cdc42 is mediated by the synergic actin-bundling activity of the Eps8-IRSp53 complex. *Nat. Cell Biol.* **8,** 1337–1347 (2006).
18. Goh, W. I. *et al.* mDia1 and WAVE2 proteins interact directly with IRSp53 in filopodia and are Involved in filopodium formation. *J. Biol. Chem.* **287,** 4702–4714 (2012).
19. Zhao, H., Pykäläinen, A. & Lappalainen, P. I-BAR domain proteins: linking actin and plasma membrane dynamics. *Curr. Opin. Cell Biol.* **23,** 14–21 (2011).
20. Ahmed, S., Goh, W. I. & Bu, W. I-BAR domains, IRSp53 and filopodium formation. *Semin. Cell Dev. Biol.* **21,** 350–356 (2010).
21. Kast, D. J. *et al.* Mechanism of IRSp53 inhibition and combinatorial activation by Cdc42 and downstream effectors. *Nat. Struct. Mol. Biol.* **21,** 413–422 (2014).
22. Scita, G., Confalonieri, S., Lappalainen, P. & Suetsugu, S. IRSp53: crossing the road of membrane and actin dynamics in the formation of membrane protrusions. *Trends Cell Biol.* **18,** 52–60 (2008).
23. Mattila, P. K. & Lappalainen, P. Filopodia: molecular architecture and cellular functions. *Nat. Rev. Mol. Cell Biol.* **9,** 446–454 (2008).
24. Yamagishi, A., Masuda, M., Ohki, T., Onishi, H. & Mochizuki, N. A novel actin bundling/filopodium-forming domain conserved in insulin receptor tyrosine kinase substrate p53 and missing in metastasis protein. *J. Biol. Chem.* **279,** 14929–14936 (2004).
25. Yang, C., Hoelzle, M., Disanza, A., Scita, G. & Svitkina, T. Coordination of membrane and actin cytoskeleton dynamics during filopodia protrusion. *PLoS ONE* **4,** e5678 (2009).
26. Sorre, B. *et al.* Nature of curvature-coupling of amphiphysin with membranes depends on its bound density. *Proc. Natl Acad. Sci. USA* **109,** 173–178 (2012).
27. Zhu, C., Das, S. & Baumgart, T. Nonlinear sorting, curvature generation, and crowding of endophilin n-bar on tubular membranes. *Biophys. J.* **102,** 1837–1845 (2012).
28. Sorre, B. *et al.* Curvature-driven lipid sorting needs proximity to a demixing point and is aided by proteins. *Proc. Natl Acad. Sci. USA* **106,** 5622–5626 (2009).
29. Tian, A. & Baumgart, T. Sorting of lipids and proteins in membrane curvature gradients. *Biophys. J.* **96,** 2676–2688 (2009).
30. Roux, A. *et al.* Membrane curvature controls dynamin polymerization. *Proc. Natl Acad. Sci.* **107,** 4141–4146 (2010).
31. Aimon, S. *et al.* Membrane shape modulates trans-membrane protein distribution. *Dev. Cell* **28,** 212–218 (2014).
32. Campillo, C. *et al.* Unexpected membrane dynamics unveiled by membrane nanotube extrusion. *Biophys. J.* **104,** 1248–1256 (2013).
33. McLaughlin, S. & Murray, D. Plasma membrane phosphoinositide organization by protein electrostatics. *Nature* **438,** 605–611 (2005).
34. Morlot, S. *et al.* Membrane shape at the edge of the dynamin helix sets location and duration of the fission reaction. *Cell* **151,** 619–629 (2012).

35. Noireaux, V. & Libchaber, A. A vesicle bioreactor as a step toward an artificial cell assembly. *Proc. Natl Acad. Sci. USA* **101,** 17669–17674 (2004).

36. Yamada, A. *et al.* Spontaneous transfer of phospholipid-coated oil-in-oil andwater-in-oil micro-droplets through an oil/water interface. *Langmuir* **22,** 9824–9828 (2006).

37. Pontani, L. -L. *et al.* Reconstitution of an actin cortex inside a liposome. *Biophys. J.* **96,** 192–198 (2009).

38. Abkarian, M., Loiseau, E. & Massiera, G. Continuous droplet interface crossing encapsulation (cDICE) for high throughput monodisperse vesicle design. *Soft Matter* **7,** 4610–4614 (2011).

39. Richmond, D. L. *et al.* Forming giant vesicles with controlled membrane composition, asymmetry, and contents. *Proc. Natl Acad. Sci. USA* **106,** 9431–9436 (2011).

40. Tsai, F. -C., Stuhrmann, B. & Koenderink, G. H. Encapsulation of active cytoskeletal protein networks in cell-sized liposomes. *Langmuir* **27,** 10061–10071 (2011).

41. Weinberger, A. *et al.* Gel-assisted formation of giant unilamellar vesicles. *Biophys. J.* **105,** 154–164 (2013).

42. Méléard, P., Bagatolli, L. A. & Pott, T. in *Methods in Enzymology*. (eds Nejat, D.) **465,** 161–176 (Academic Press, 2009).

43. Angelova, M. I., Soléau, S., Méléard, P., Faucon, J. F. & Bothorel, P. Preparation of giant vesicles by external AC electric fields. Kinetics and applications. *Prog. Coll. Pol. Sci.* **89,** 127–131 (1992).

44. Carvalho, K., Ramos, L., Roy, C. & Picart, C. Giant unilamellar vesicles containing phosphatidylinositol(4,5)bisphosphate: characterization and functionality. *Biophys. J.* **95,** 4348–4360 (2008).

45. Rodriguez, N., Pincet, F. & Cribier, S. Giant vesicles formed by gentle hydration and electroformation: a comparison by fluorescence microscopy. *Colloids Surf. B Biointerfaces* **42,** 125–130 (2005).

46. Ramesh, P. *et al.* FBAR Syndapin 1 recognizes and stabilizes highly curved tubular membranes in a concentration dependent manner. *Sci. Rep.* **3,** 1565 (2013).

47. Shlomovitz, R., Gov, N. S. & Roux, A. Membrane-mediated interactions and the dynamics of dynamin oligomers on membrane tubes. *New J. Phys.* **13,** 065008 (2011).

48. Bozic, B., Das, S. L. & Svetina, S. Sorting of integral membrane proteins mediated by curvature-dependent protein-lipid bilayer interaction. *Soft Matter* **11,** 2479–2487 (2015).

49. Gov, N. S. & Gopinathan, A. Dynamics of membranes driven by actin polymerization. *Biophys. J.* **90,** 454–469 (2006).

50. Shlomovitz, R. & Gov, N. S. Membrane-mediated interactions drive the condensation and coalescence of FtsZ rings. *Phys. Biol.* **6,** 046017 (2009).

51. Derényi, I., Jülicher, F. & Prost, J. Formation and interaction of membrane tubes. *Phys. Rev. Lett.* **88,** 238101 (2002).

52. Saarikangas, J. *et al.* MIM-induced membrane bending promotes dendritic spine initiation. *Dev. Cell* **33,** 644–659 (2015).

53. Singh, P., Mahata, P., Baumgart, T. & Das, S. L. Curvature sorting of proteins on a cylindrical lipid membrane tether connected to a reservoir. *Phys. Rev. E Stat. Nonlin. Soft Matter Phys.* **85,** 051906 (2012).

54. Khelashvili, G., Harries, D. & Weinstein, H. Modeling Membrane deformations and lipid demixing upon protein-membrane interaction: the BAR dimer adsorption. *Biophys. J.* **97,** 1626–1635 (2009).

55. Frost, A. *et al.* Structural basis of membrane invagination by F-BAR domains. *Cell* **132,** 807–817 (2008).

56. Mim, C. *et al.* Structural basis of membrane bending by the N-BAR protein endophilin. *Cell* **149,** 137–145 (2012).

57. Zhao, H. *et al.* Membrane-sculpting BAR domains generate stable lipid microdomains. *Cell Rep.* **4,** 1213–1223 (2013).

58. Picas, L. *et al.* BIN1/M-Amphiphysin2 induces clustering of phosphoinositides to recruit its downstream partner dynamin. *Nat. Commun.* **5,** 5647 (2014).

59. Lee, K., Gallop, J. L., Rambani, K. & Kirschner, M. W. Self-assembly of filopodia-like structures on supported lipid bilayers. *Science* **329,** 1341–1345 (2010).

60. Henne, W. M. *et al.* FCHo proteins are nucleators of clathrin-mediated endocytosis. *Science* **328,** 1281–1284 (2010).

61. Schneider, K. *et al.* ProSAP1 and membrane nanodomain-associated syndapin I promote postsynapse formation and function. *J. Cell Biol.* **205,** 197–215 (2014).

62. Kwok, R. & Evans, E. Thermoelasticity of large lecithin bilayer vesicles. *Biophys. J.* **35,** 637–652 (1981).

63. Neuman, K. C. & Block, S. M. Optical trapping. *Rev. Sci. Instrum.* **75,** 2787–2809 (2004).

64. Gov, N. S. & Gopinathan, A. Dynamics of membranes driven by actin polymerization. *Biophys. J.* **90,** 454–469 (2006).

Acknowledgements

Author contributions

P.B. conceived the project. C.P. generated and analysed the data of reconstituted *in vitro* experiments. A.C.J. provided the theoretical model and analysis. C.P., J.M. and H.Z. performed protein purification. C.P., E.L., P.L., A.C.J. and P.B. wrote the manuscript.

Additional information

Supplementary Information accompanies this paper at http://www.nature.com/naturecommunications

Competing financial interests: The authors declare no competing financial interests.

Reprints and permission information is available online at http://npg.nature.com/reprintsandpermissions/

How to cite this article: Prévost, C. *et al.* IRSp53 senses negative membrane curvature and phase separates along membrane tubules. *Nat. Commun.* 6:8529 doi: 10.1038/ncomms9529 (2015).